Supporting Information

Efficient solid-state photoswitching of methoxyazobenzene in a metal-organic framework for thermal energy storage.

Kieran Griffiths[†], Nathan R. Halcovitch[†], John M. Griffin[†‡*]

† Department of Chemistry, Lancaster University, Lancaster, LA1 4YB, UK

‡ Materials Science Institute, Lancaster University, Lancaster, LA1 4YB, UK

Table of Contents

Experimental Details

Synthesis of 1. All reagents were obtained from Fluorochem and used without further purification. $Zn_2(BDC)_2(DABCO)$ was synthesised according to previously reported synthetic procedures. $Zn(NO_3)_2 \cdot 6H_2O$ (1.68 mmol) was sonicated in N,N-dimethylformamide (DMF, 20 mL) until fully dissolved, 1,4-dibenzendicarboxylic acid (0.28 g, 1.68 mmol) and DABCO (0.093 g, 0.84 mmol) were then added. The reactant solution was placed in a stainless-steel autoclave (Parr) with a Teflon lining with a 50 mL capacity. The solution was heated at 120 °C for 48 h and left to cool to room temperature. The colourless crystals (yield - 81%) were collected via vacuum filtration and washed with DMF (3 x 30 mL) before drying under ambient conditions. Phase purity of the compounds was confirmed by Le Bail fitting of the XRPD patterns.

Loading of 1 with MOAB. Samples of **1** were loaded with MOAB using a previously published melt-infiltration procedure. As-prepared samples of **1** were first heated at 120 °C under vacuum for 24 h to remove DMF solvent molecules. 300 mg of the evacuated material was then mixed with a defined mass of *E*-MOAB and heated at 120 °C for 3 h. Excess MOAB was removed by heating at 120 °C under vacuum for 20 h.

Quantification of MOAB loading level by UV-vis spectroscopy. UV-vis data was collected on a Cary 60 UV/VIS spectrophotometer with a quartz cell (3 mL) within a 200-600 nm range. A calibration curve with known concentrations of *E*-MOAB was constructed (see Figures S1 and S2).

Quantification of loading level by acid digestion and ^{1}H NMR spectroscopy. 10 mg of **1**⊃MOAB was suspended in DCl (1.5 mL) and DMSO-d_6 (1.5 mL) and placed in a stainless-steel autoclave (Parr) with a Teflon lining with a 50 mL capacity. The suspension was heated for 12 h at 100 °C to yield a transparent solution. A Bruker Avance III 400 NMR spectrometer with a 5 mm ^{1}H-X broadband observe probe was used to collected ^{1}H NMR data. The ^{1}H NMR spectrum of the solution was taken and the ratio between DABCO, BDC and E-MOAB was determined from the integration of characteristic ^{1}H resonances.

PSS determination of irradiated 1⊃MOAB composites. A 25 mg sample of **1**⊃MOAB was suspended in benzene-d_6 (0.5 mL) in an Eppendorf and shaken. The Eppendorf was centrifuged to separate the solid from the solution. A Bruker Avance III 400 NMR spectrometer with a 5 mm ^{1}H-X broadband observe probe was used to collect ^{1}H NMR data. The population ratio of *E*-MOAB and *Z*-MOAB isomers was determined from integration of *Z*-isomer and *E*-isomer resonances in the ^{1}H NMR spectrum based on literature values. The remaining solid was digested in DCl (1.5 mL) and DMSO-d_6 (1.5 mL) and placed in a stainless-steel autoclave (Parr) with a Teflon lining with a 50 mL capacity. The suspension was heated for 12 h at 100 °C to yield a transparent solution. The ^{1}H NMR spectrum of the solution was taken, and no residual *Z*-MOAB or *E*-MOAB resonances were detected. The process was repeated three separate times and *E/Z* ratios were consistent.

UV light irradiation procedure. Samples were irradiated with an OmniCure LX5 LED Head with a power of 425 mW and a 12 mm focusing lens. 50 mg of finely ground **1**⊃MOAB was spread homogenously over a microscope slide. The powder was spread into a circle with a 1 cm radius which was approximately 0.5 mm thick so that irradiation was approximately uniform. The irradiance at central point was 0.3 W cm^{-2}. The slide was placed under 365 nm light at a distance of 5 cm. The beam was set to 100% intensity and exposed for a fixed duration. The sample was agitated, at increments of 5 minutes, to allow all particulates to be exposed to the beam.

XRPD. X-ray powder diffraction (XRPD) patterns were measured with a Rigaku SmartLab X-ray diffractometer with a 9 kW rotating anode Cu-source equipped with a high-resolution Vertical θ/θ 4-Circle Goniometer and D/teX-ULTRA 250 High-Speed Position-Sensitive Detector System in reflectance mode. The system was configured with parallel-beam optics and a Ge(220) 2 bounce monochromator on the incident side. Powdered solid samples were prepared on glass slides. The measurements were performed as θ/2θ scans with a step size of 0.01 degrees. Variable-temperature measurements were carried out by loading the powder sample into 1 mm diameter thin-walled (0.1mm) borosilicate capillaries, with the capillary loosely sealed with silicone grease to allow for pressure to be released upon heating. The capillary was loaded on a BTS-500 Anton Parr heating stage equipped with a zero-background holder and mounted on a Rigaku SmartLab (9 kW) diffractometer. The heating stage was purged with nitrogen for 30 minutes prior to analysis. The diffractometer was used with parallel-beams optics and a 5 degree soller slit, and a Dtex-250 Ultra 1D detector. The sample run was carried out using a 2-theta scan with a step size of 0.01 degrees 2-theta, and a scanning rate of 4 degrees per minute.

Solid-state NMR. Solid-state NMR experiments were performed on Bruker Avance III HD spectrometer operating at magnetic field strength of 16.4 T, corresponding to ^{1}H and ^{13}C Larmor frequencies of 700 and 176 MHz, respectively. Spectra are referenced relative to tetramethylsilane (^{13}C / ^{1}H) using the CH_3 (^{1}H = 1.1 ppm; ^{13}C = 20.5 ppm) resonances of *L*-alanine as a secondary reference. ^{13}C NMR spectra were recorded at a magic-angle spinning (MAS) rate of 16.0 kHz using cross polarization (CP) to transfer magnetization from ^{1}H with a contact time of 3 ms. The CP pulse was ramped linearly from 70 – 100% power. ^{1}H heteronuclear decoupling using two-pulse phase modulation (TPPM)[45] with a pulse length of 4.8 μs and a radiofrequency field strength of 100 kHz was applied during acquisition. Spectra are the sum of 512 transients separated by a recycle interval of 10 s. The sample temperature in variable-temperature experiments was calibrated using $Pb(NO_3)_2$.[46]

DFT Calculation Details

First-principles calculations of NMR parameters were carried out under periodic boundary conditons using the CASTEP code[1] employing the gauge-including projector augmented wave (GIPAW) algorithm,[2] which allows the reconstruction of the all-electron wave function in the presence of a magnetic field. The CASTEP calculations employed the generalised gradient approximation Perdew–

Burke–Ernzerhof exchange-correlation functional,[3] and core–valence interactions were described by ultrasoft pseudopotentials.[4]

Prior to calculation of the NMR parameters, structures were fully geometry optimised using the G06 semiempirical dispersion correction scheme[5] and allowing all atomic positions to vary. For calculations on guest-free frameworks, the input atomic co-ordinates were taken from structures published by Dybtsev *et al*., with the guest molecule atoms deleted where appropriate.[6] The tetragonal *lp* structure was based on the empty framework structure, the orthorhombic *np* structure was based on the benzene-loaded structure, and the distorted tetragonal np structure was based on the DMF-loaded structure. These structures also required deletion of some of the atoms representing the dynamic disorder of the DABCO group in order to make a chemically sensible input structure. The structures were then optimized while keeping the unit cell parameters fixed to the experimental values.

Single-molecule calculations were carried out in a 20 × 20 × 20 Å cell with fixed cell parameters to ensure molecules remained isolated from periodic replicas.

Geometry optimisations and NMR calculations were carried out using a planewave energy cut-off of 60 Ry, and for crystal structures, a k-point spacing of 0.05 2π $Å^{-1}$ was used. For single-molecule calculations, a single k-point at the fractional coordinate (0.25, 0.25, 0.25) was used. The calculations generate the absolute shielding tensor (σ) in the crystal frame. Diagonalisation of the symmetric part of σ yields the three principal components, σ_{XX}, σ_{YY}, and σ_{ZZ}. The isotropic shielding, σ_{iso}, is given by (1/3) Tr [σ]. The iso- tropic chemical shift, δ_{iso}, is given by $\sigma_{ref} - \sigma_{iso}$, where σ_{ref} is a reference shielding. Reference shieldings were determined by comparison of experimental chemical shifts for *L*-alanine with shieldings obtained from a calculation on a fully optimised crystal structure[7] (Cambridge Structural Database code LALNIN22). For ^{1}H and ^{13}C, reference shieldings were determined from the *y* intercept of a linear fit to the experimental shifts versus calculated shielding, with the gradient of the fit fixed to −1. Calculated shieldings for the three methyl protons were averaged to account for rapid rotation of the methyl group. Respective reference shieldings of 30.2 and 168.4 ppm were obtained for ^{1}H and ^{13}C. Calculated chemical shifts for the individual carbons in DABCO groups were averaged to account for the fast rotational dynamics of this group.

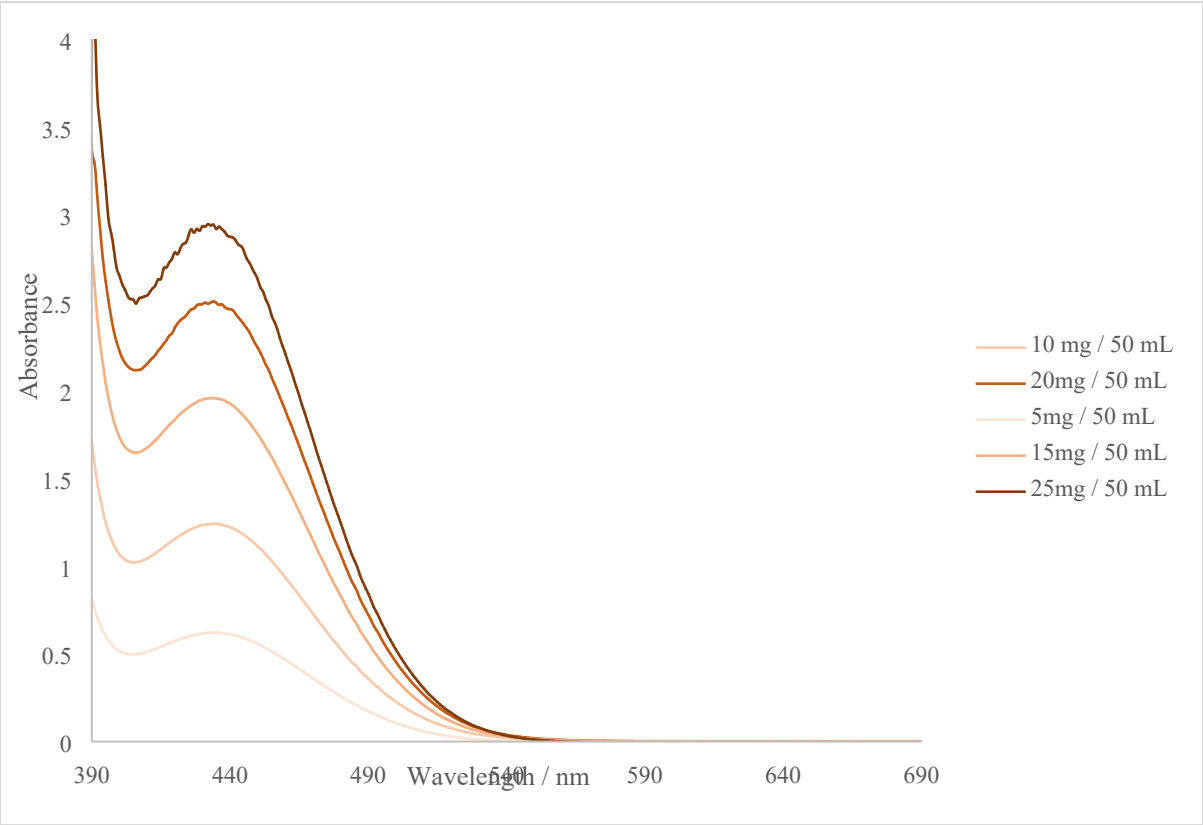

Figure S1. UV-Vis spectra for increasing concentrations of *E*-MOAB in MeOH.

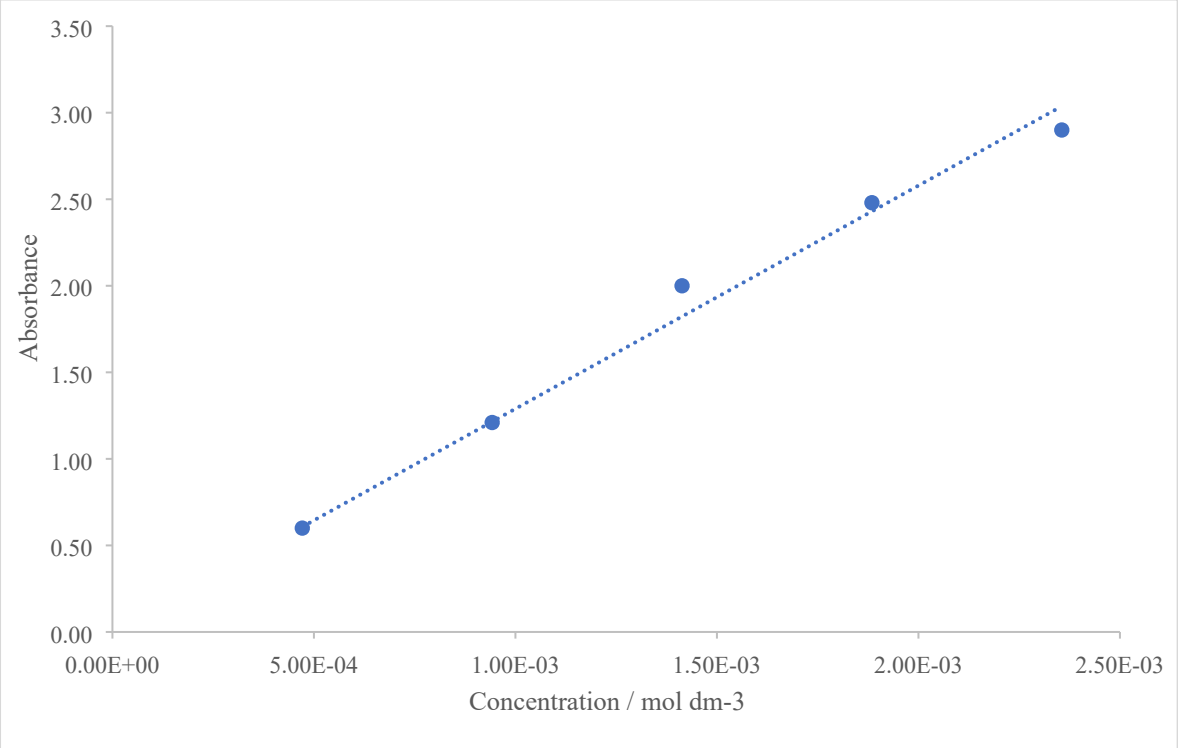

Figure S2. UV-Vis Calibration curve for *E*-MOAB in MeOH.

Table S1. Table for the calibration curve for *E*-MOAB.

mass / mg	mass / g	Moles / mol	concentration /mol dm^{-3}	Absorbance
5	0.005	0.000023557	4.71E-04	0.60
10	0.01	0.000047114	9.42E-04	1.21
15	0.015	0.000070671	1.41E-03	2.00
20	0.02	0.000094229	1.88E-03	2.48
25	0.025	0.000117786	2.36E-03	2.90

Table S2. Determination of the number of moles of *E*-MOAB in **1**⊃MOAB (25mL of MeOH).

Entry	Mass of **1**MOAB / mg	mass / g	Absorbance	Concentration /mol dm^{-3}	Moles / mol	mass of MOAB / g	mass / mg
1	19.8	0.0198	1.53	0.001185587	0.0000296397	0.006291021	6.291020922
2	18.7	0.0187	1.46	0.001131344	0.0000282836	0.006003196	6.003196435
3	19.3	0.0193	1.48	0.001146842	0.0000286711	0.006085432	6.085432003
							6.126549787

Table S3. Determination of the ratio of **1** to *E*-MOAB in **1**⊃MOAB.

Entry	Mass of 1 /mg	Mass of **1** / g	mol of **1** / mol	mol of MOAB	Ratio **1**	Ratio MOAB
1	13.50897908	0.013508979	0.000023650588	0.0000296397	1	1.253232062
2	12.69680356	0.012696804	0.000022228687	0.0000282836	1	1.272392353
3	13.214568	0.013214568	0.000023135153	0.0000286711	1	1.239285421
						1.254969945

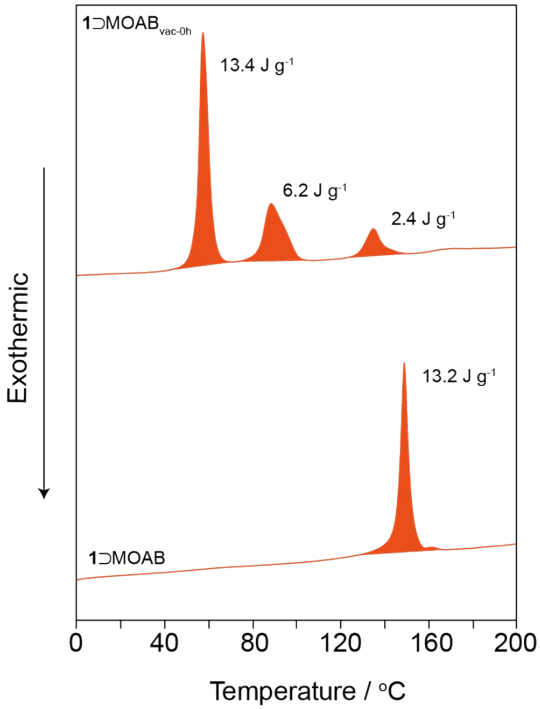

Figure S3. DSC thermograms of **1**⊃MOAB and **1**⊃MOAB pre-vacuum treatment. Endothermic transitions below 100 °C are melting transitions for polymorphs of MOAB. These are absent from **1**⊃MOAB.

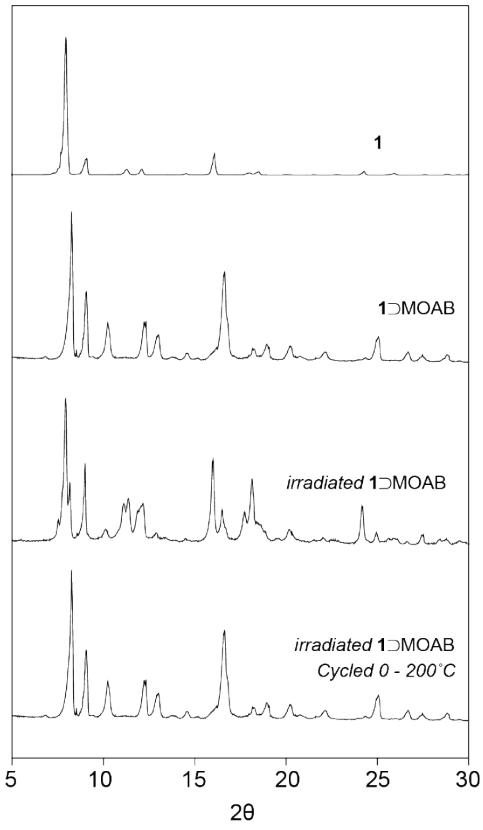

Figure S4. XRPD comparison for **1**⊃MOAB composites.

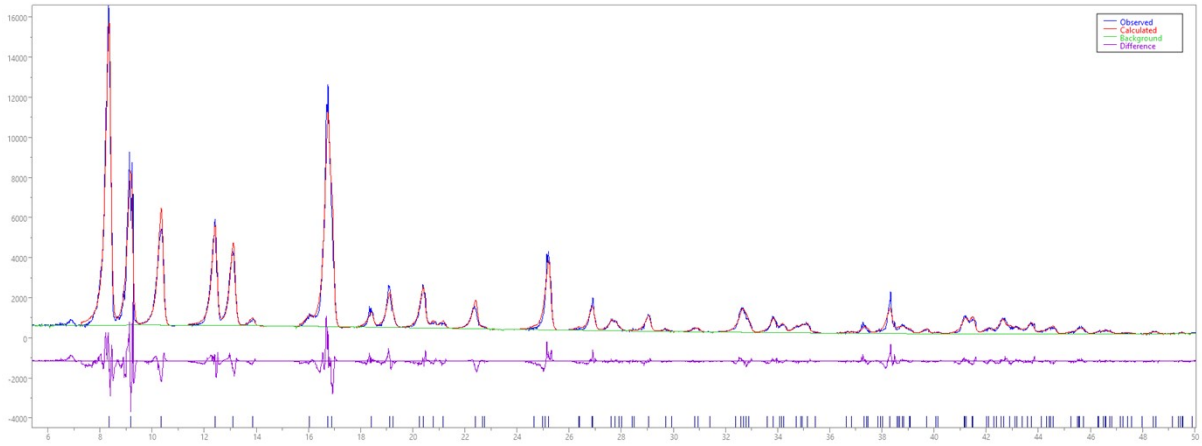

Figure S5. Le Bail fit of **1**⊃MOAB. The crystal system was found to be orthorhombic. The lattice parameters were refined to be a =13.492(2) Å, b = 17.129(4), c = 9.679(8) Å, $a = b = g = 90°$, V = 2236.9(3) Å^3. The space group was found to be *Cmmm*. General formula $Zn_8C_{128}H_{120}N_{16}O_{32}$. The reliability (R) factor based on the powder profile *Rp* was 8.65 %.

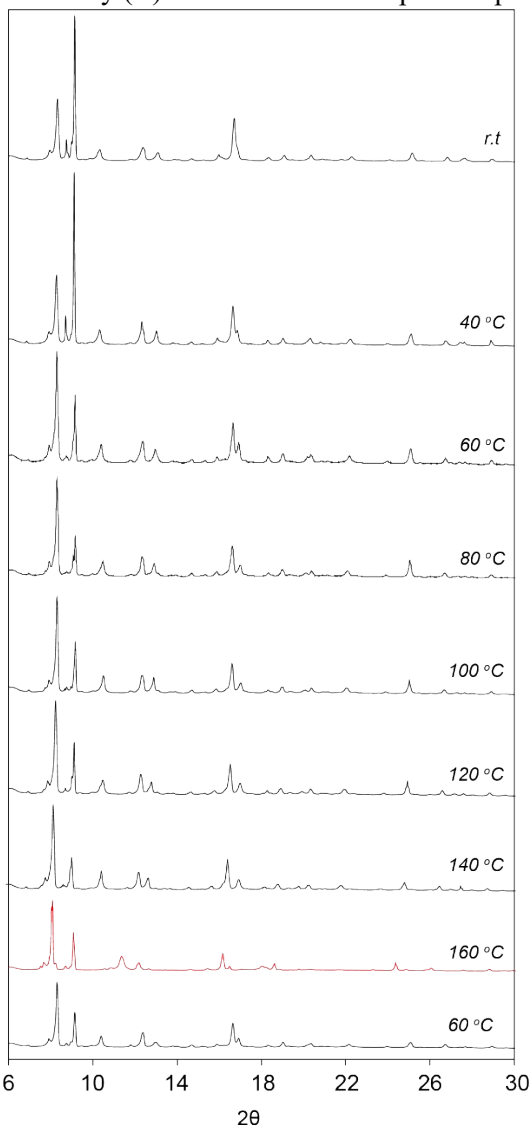

Figure S6. VT-PXRD patterns for **1**⊃MOAB.

Table S4. Temperature-dependent unit cell lengths for the *Cmmm* (*np*) phase of **1**⊃MOAB, brackets indicate axes converted from *P4/mmm* (lp) phase.

Temperature / °C	*a* / Å	*b* / Å	*c* / Å	V / Å^3
20	13.492	17.129	9.679	2236.9
40	13.566	17.105	9.681	2246.4
60	13.629	17.049	9.679	2249.0
80	13.701	16.944	9.672	2245.4
100	13.754	16.855	9.681	2244.3
120	13.788	16.768	9.681	2238.2
140	13.802	16.703	9.681	2231.8
[160]	[15.501]	[15.501]	[9.706]	[2332.2]
[180]	[15.501]	[15.501]	[9.706]	[2332.2]

Table S5. Temperature-dependent unit cell expansion/ contraction for the *Cmmm* (*np*) phase of **1**⊃MOAB, brackets indicate axes converted from *P4/mmm* (*lp*) phase.

Temperature	*a* expansion / %	*b* contraction / %	*c* / %	V / %
20	0.00	0.00	0.00	0.00
40	0.55	-0.14	0.02	0.42
60	1.02	-0.47	0.00	0.55
80	1.55	-1.08	-0.37	0.61
100	1.94	-1.60	0.02	0.33
120	2.20	-2.11	0.02	0.06
140	2.30	-2.49	-0.50	-0.23
[160]	[14.9]	[-9.50]	[0.27]	[4.26]
[180]	[14.9]	[-9.50]	[0.27]	[4.26]

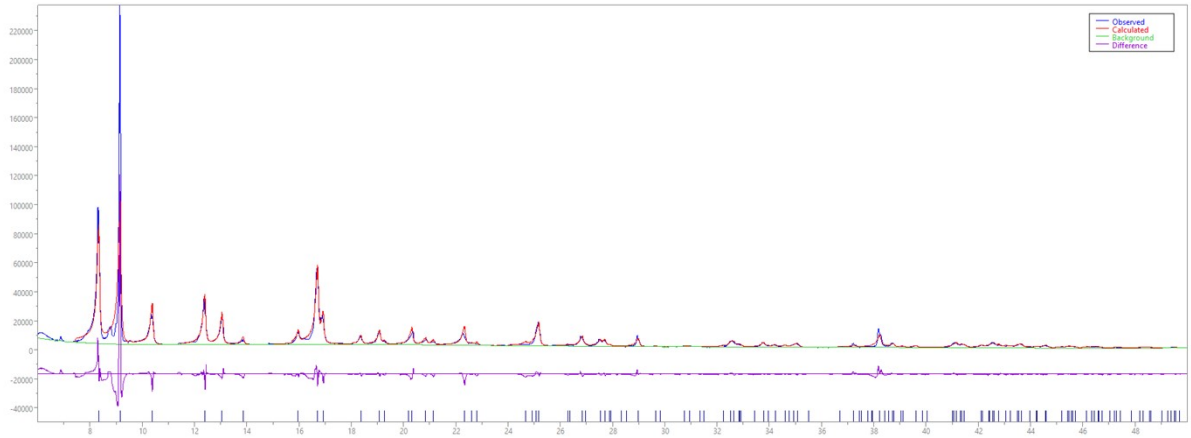

Figure S7. Le Bail fit of **1**⊃MOAB at 40 °C. The crystal system was found to be orthorhombic. The lattice parameters were refined to be *a* =13.566(3) Å, *b* = 17.105(2), *c* = 9.681 (7) Å, $\alpha = \beta = \gamma = 90°$, V = 2246.4(4) Å^3. The space group was found to be *Cmmm*. General formula $Zn_8C_{128}H_{120}N_{16}O_{32}$. The reliability (R) factor based on the powder profile *Rp* was 8.99 %.

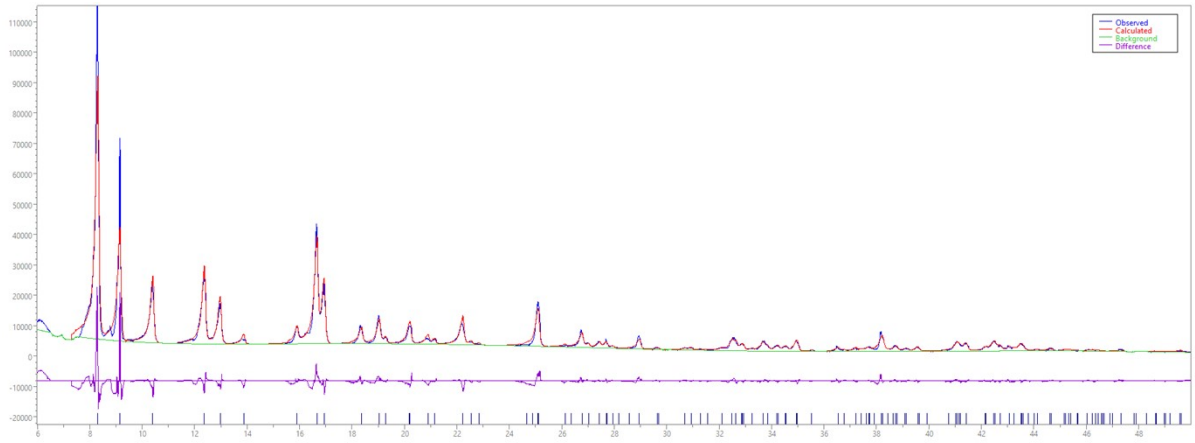

Figure S8. Le Bail fit of **1**⊃MOAB at 60 °C. The crystal system was found to be orthorhombic. The lattice parameters were refined to be a =13.629(4) Å, b = 17.049 (3), c = 9.679 (5) Å, $\alpha = \beta = \gamma = 90°$, V = 2249.0(4) Å^3. The space group was found to be *Cmmm*. General formula $Zn_8C_{128}H_{120}N_{16}O_{32}$. The reliability (R) factor based on the powder profile *Rp* was 8.12 %.

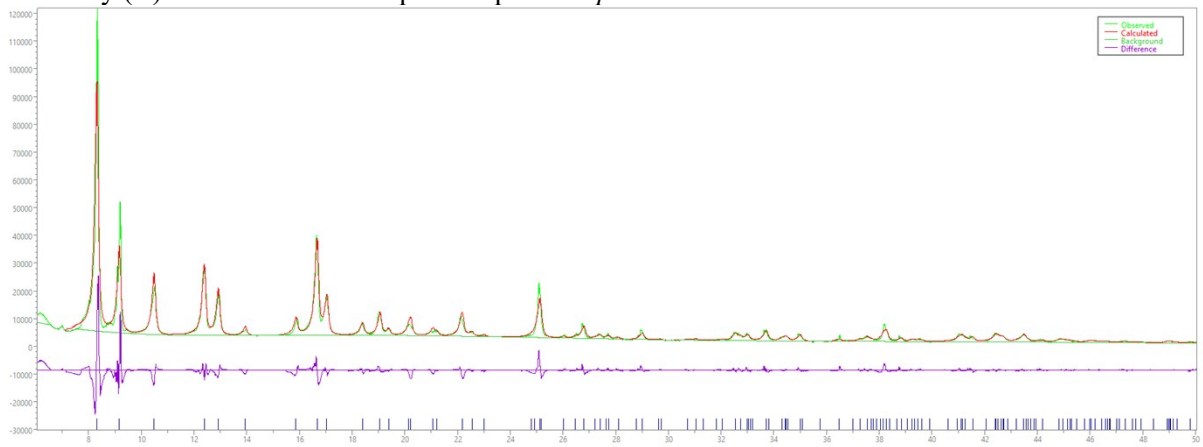

Figure S9. Le Bail fit of **1**⊃MOAB at 80 °C. The crystal system was found to be orthorhombic. The lattice parameters were refined to be a =13.701(2) Å, b = 16. 944(3), c = 9.672 (5) Å, $\alpha = \beta = \gamma = 90°$, V = 2245.4(4) Å^3. The space group was found to be *Cmmm*. General formula $Zn_8C_{128}H_{120}N_{16}O_{32}$. The reliability (R) factor based on the powder profile *Rp* was 7.01 %.

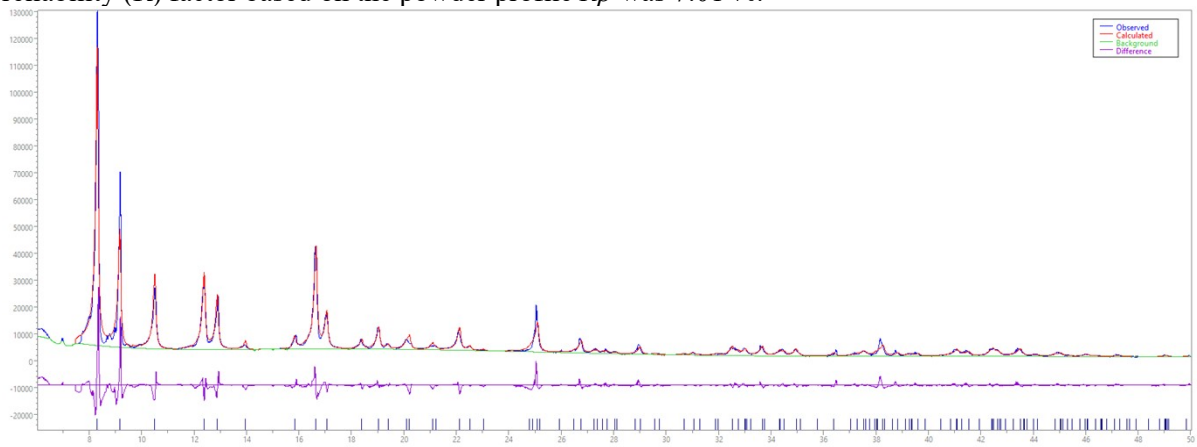

Figure S10. Le Bail fit of **1**⊃MOAB at 100 °C. The crystal system was found to be orthorhombic. The lattice parameters were refined to be a =13.754(3) Å, b = 16.855(3), c = 9.681 (6) Å, $\alpha = \beta = \gamma = 90°$, V = 2244.3(4) Å^3. The space group was found to be *Cmmm*. General formula $Zn_8C_{128}H_{120}N_{16}O_{32}$. The reliability (R) factor based on the powder profile *Rp* was 5.11 %.

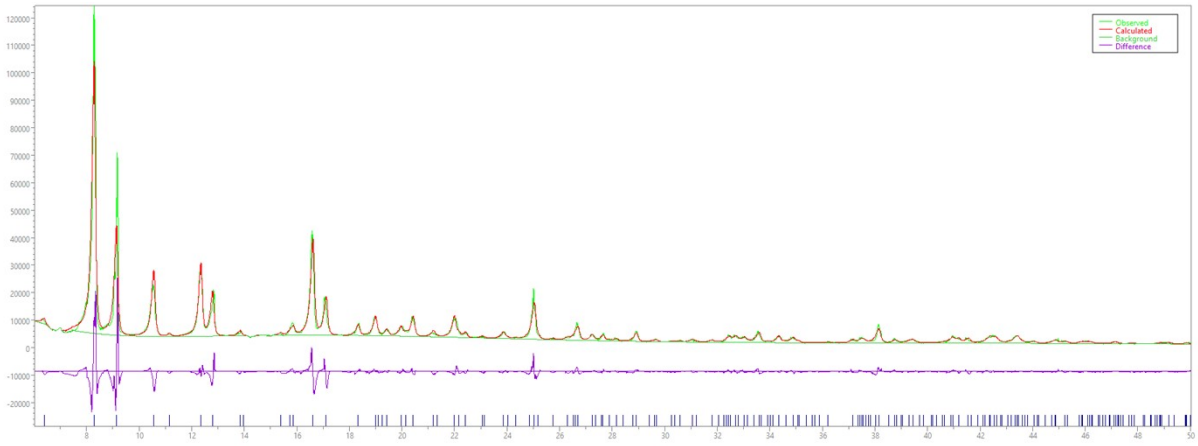

Figure S11. Le Bail fit of **1**⊃MOAB at 120 °C. The crystal system was found to be orthorhombic. The lattice parameters were refined to be a =13.788(4) Å, b = 16.768(3), c = 9.681 (5) Å, $\alpha = \beta = \gamma = 90°$, V = 2240.4(6) Å^3. The space group was found to be *Cmmm*. General formula $Zn_8C_{128}H_{120}N_{16}O_{32}$. The reliability (R) factor based on the powder profile *Rp* was 7.95 %.

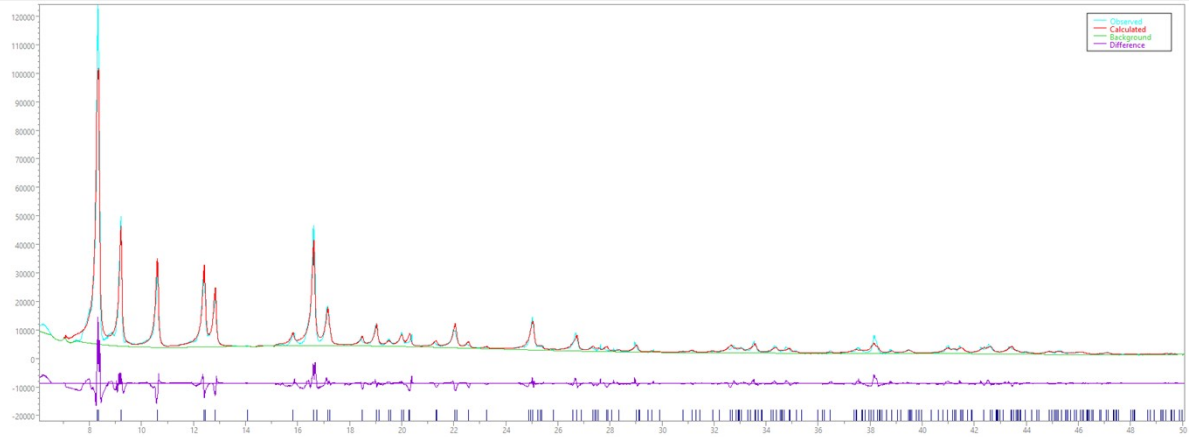

Figure S12. Le Bail fit of **1**⊃MOAB at 140 °C. The crystal system was found to be orthorhombic. The lattice parameters were refined to be a =13.801(2) Å, b = 16.703(2), c = 9.681 (4) Å, $\alpha = \beta = \gamma = 90°$, V = 2231.8(8) Å^3. The space group was found to be *Cmmm*. General formula $Zn_8C_{128}H_{120}N_{16}O_{32}$. The reliability (R) factor based on the powder profile *Rp* was 6.57 %.

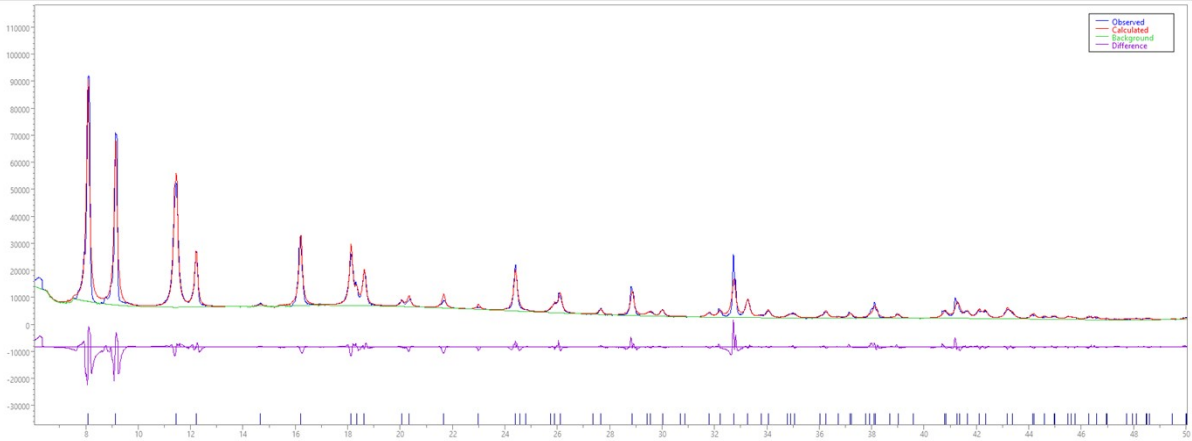

Figure S13a. Le Bail fit of **1**⊃MOAB at 160 °C. The crystal system was found to be tetragonal. The lattice parameters were refined to be $a = b$ = 10.961(3) Å, c = 9.706(2) Å, $\alpha = \beta = \gamma = 90°$, V = 1166.12(4) Å^3. The space group was found to be *P4/mmm*. General formula $Zn_4C_{64}H_{60}N_8O_{16}$. The reliability (R) factor based on the powder profile *Rp* was 6.95 %.

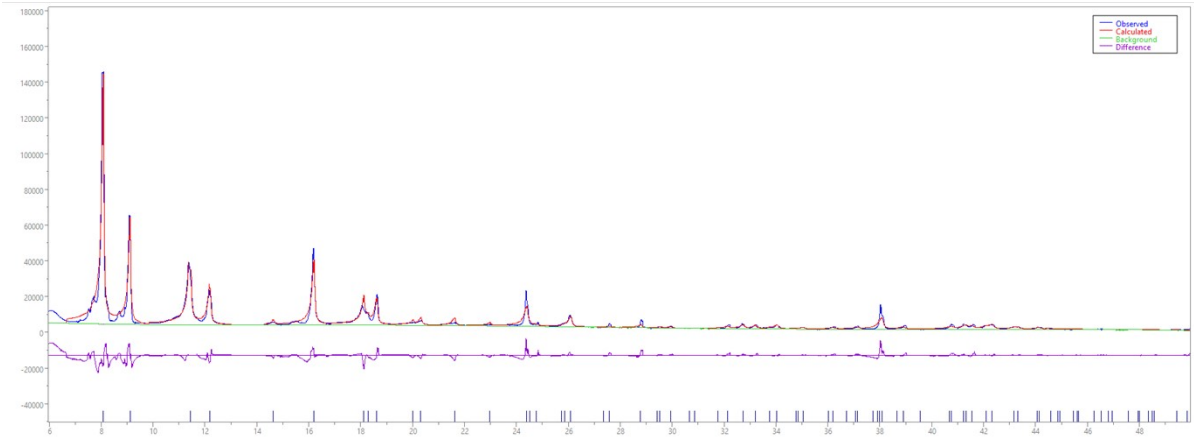

Figure S13b. Le Bail fit of **1**⊃MOAB at 180 °C. The crystal system was found to be tetragonal. The lattice parameters were refined to be $a = b = 10.961(4)$ Å, $c = 9.706(5)$ Å, $\alpha = \beta = \gamma = 90°$, V = 1166.12(6) Å^3. The space group was found to be *P4/mmm*. General formula $Zn_4C_{64}H_{60}N_8O_{16}$. The reliability (R) factor based on the powder profile *Rp* was 8.91 %.

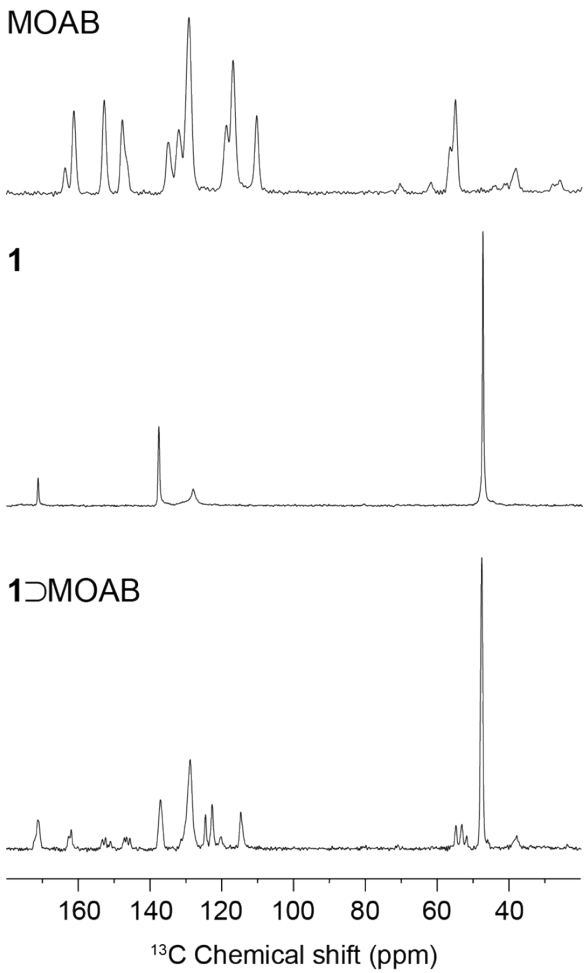

Figure S14. ^{13}C CPMAS NMR spectra comparing the chemical shifts of **1**, MOAB and of **1**⊃MOAB.

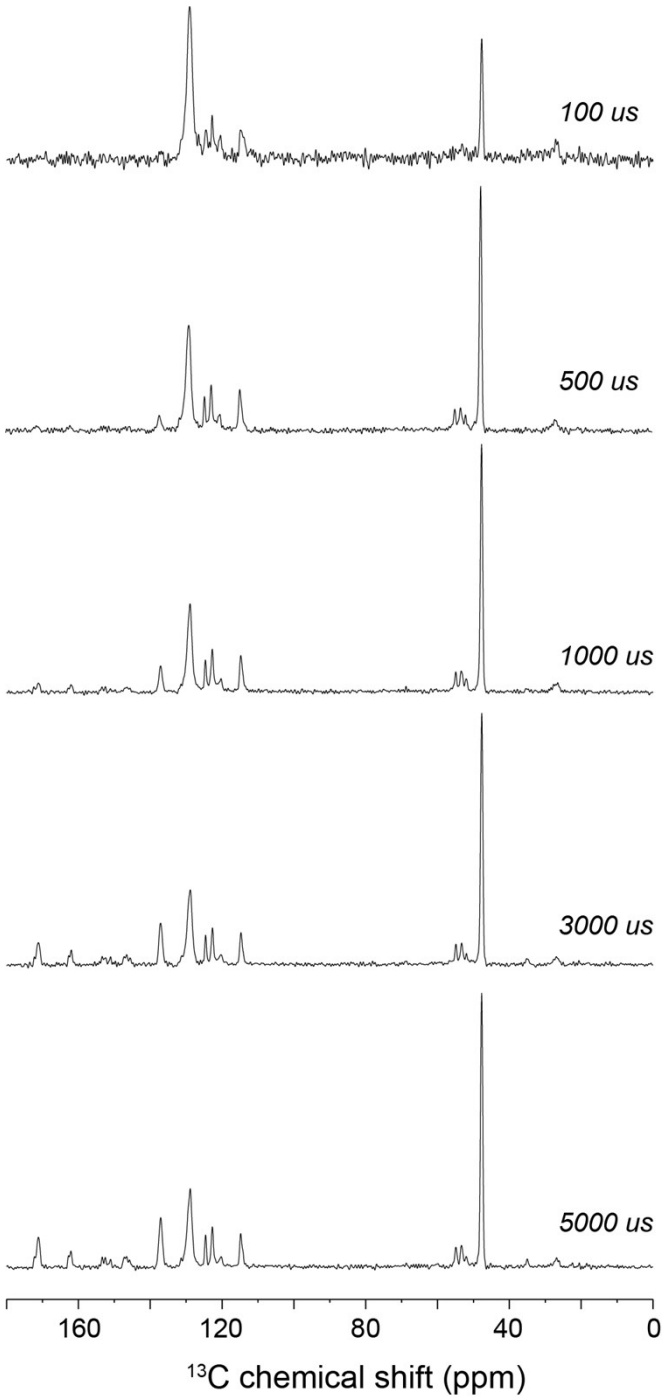

Figure S15. ^{13}C CPMAS NMR spectra of **1**⊃MOAB recorded with different cross-polarisation contact times.

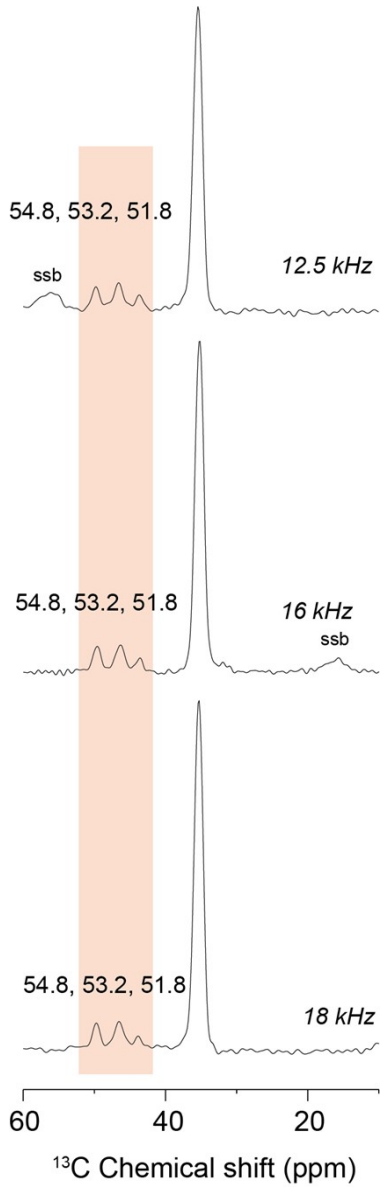

Figure S16. ^{13}C CPMAS NMR spectra of **1**⊃MOAB between 10 – 60 ppm at different MAS frequencies. This confirms the features seen at 51.8 ppm, 53.2 ppm and 54.8 ppm are from the methoxy carbon of MOAB.

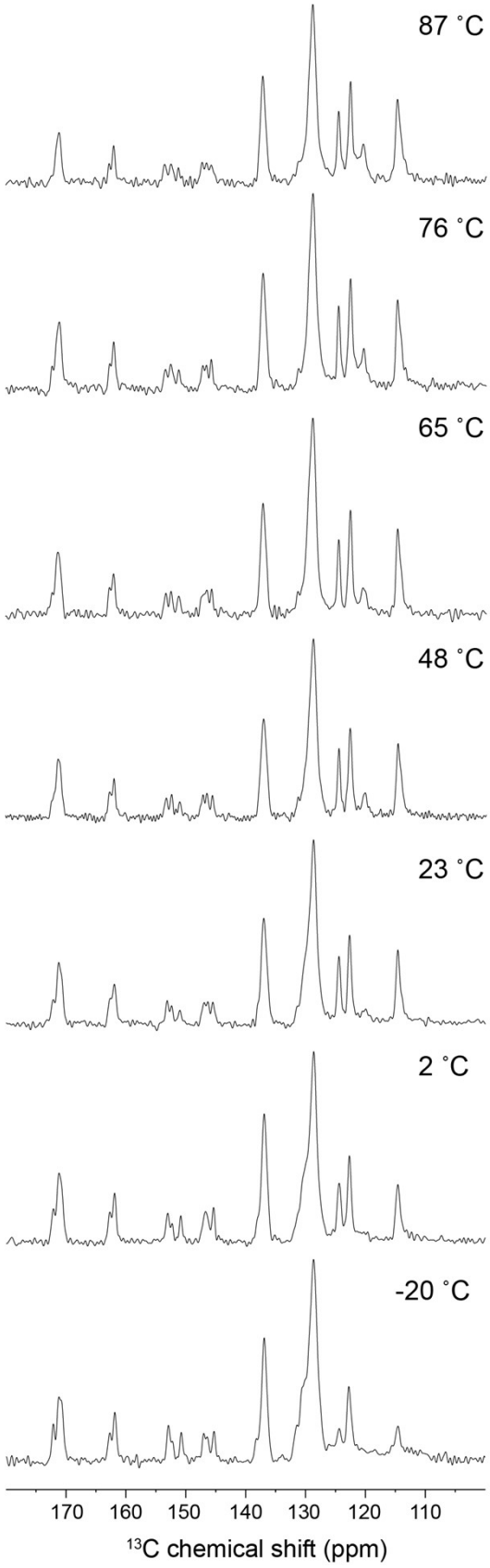

Figure S17. Variable temperature ^{13}C CPMAS NMR spectra of **1**⊃MOAB between 110 – 180 ppm.

Table S6. Calculated chemical shifts for a static molecule of *E*-MOAB. The CASTEP code was used to geometry-optimise a single molecule within a unit cell with fixed dimensions of 12 x 12 x 12 Å before NMR parameters were calculated.

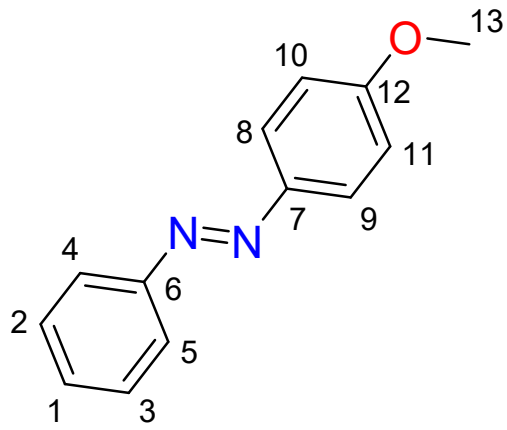

C site	σ_{iso}	Chemical shift / ppm
1	39.8602	128.5998
2	41.931	126.529
3	41.4416	127.0184
4	58.6355	109.8245
5	35.2049	133.2551
6	15.6751	152.7849
7	21.1183	147.3417
8	32.5399	135.9201
9	56.5976	111.8624
10	63.7801	104.6799
11	52.9204	115.5396
12	4.8127	163.6473
13	118.1348	50.3252

Table S7. CASTEP calculated chemical shifts for *E*-MOAB assuming fast rotational averaging around the central molecular axis

C site	σ_{iso}	Chemical shift / ppm
C1	39.8602	128.5998
C2/C3	41.6863	126.7737
C4/C5	46.9202	121.5398
C6	15.6751	152.7849
C7	21.1183	147.3417
C8/C9	44.56875	123.89125
C10/ C11	58.35025	110.10975
C12	4.8127	163.6473
C13	118.1348	50.3252

Fast rotational averaging was accounted for by averaging chemical shifts for carbons on opposite sides of the six-membered rings. This simulates the effect of fast rotation of the six-membered rings around the C-N bond. In terms of the predicted chemical shifts, this averaging is also equivalent to

fast pedal motion dynamics of the central N=N linkage – indeed rotation of the rings and pedal motion of the N=N linkage cannot be distinguished by this method.

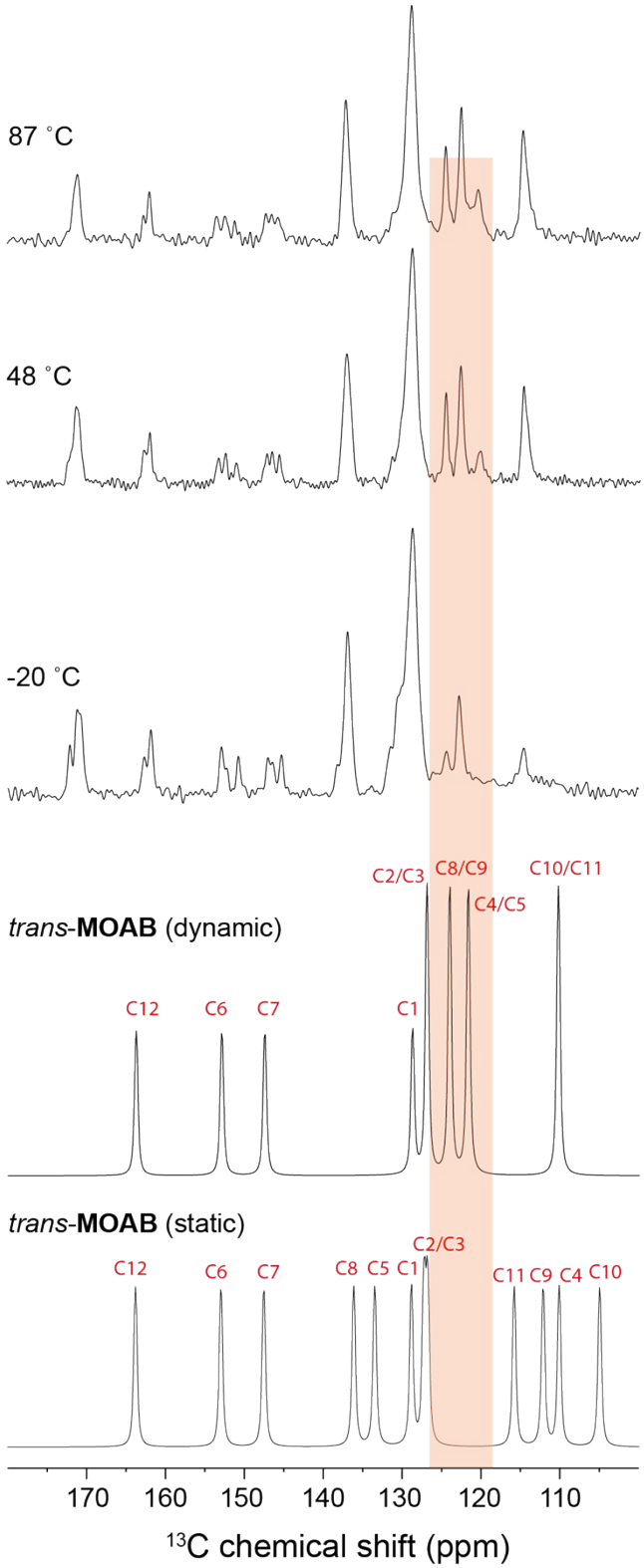

Figure S18. Variable-temperature ^{13}C CPMAS NMR spectra of **1**⊃MOAB which are compared to the calculated ^{13}C chemical shifts of *E*-MOAB. Static and dynamic models for the *E*-MOAB molecule are shown.

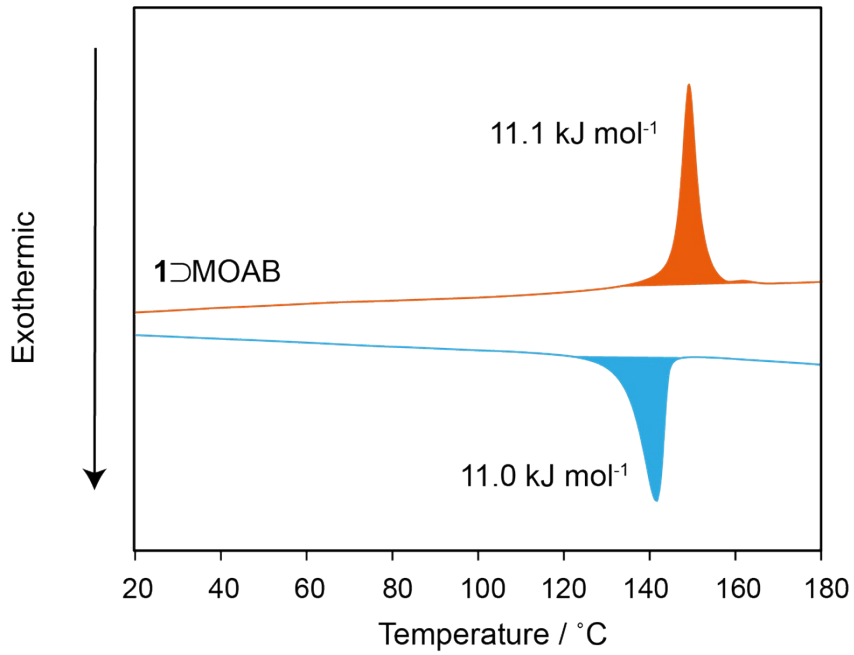

Figure S19. DSC thermogram of **1**⊃MOAB at a rate of 20 °C min^{-1}.

Table S8. Thermal data for the first heating branch of **1**⊃MOAB between 0 – 180 °C at varying heating rates.

Heating Rate / °C min^{-1}	Energy density/ J g^{-1}	Endotherm onset / °C	Endotherm peak / °C	Peak Range / °C
20	13.2	145.4	149.0	38
15	13.1	141.8	144.8	36
10	13.4	141.9	144.4	22
5	13.2	141.9	144.0	20
2.5	13.5	142.0	143.6	20

Table S9. Thermal data for the first cooling branch of **1**⊃MOAB between 0 – 180 °C at varying cooling rates.

Cooling Rate / °C min^{-1}	Energy density/ J g^{-1}	Exotherm onset / °C	Exotherm peak / °C	Peak Range / °C
20	12.7	144.2	141.3	28
15	13.0	141.1	138.7	35
10	12.2	140.9	138.8	23
5	12.5	140.7	139.2	24
2.5	12.4	140.7	139.5	36

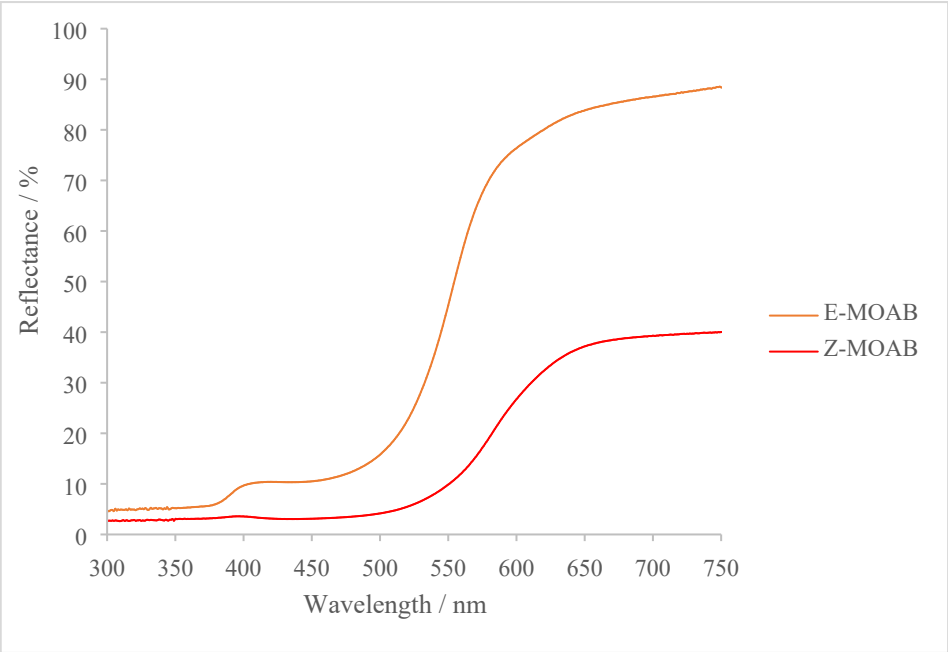

Figure S20. Solid-state UV-Vis diffuse reflectance spectra of *E*-MOAB and *Z*-MOAB.

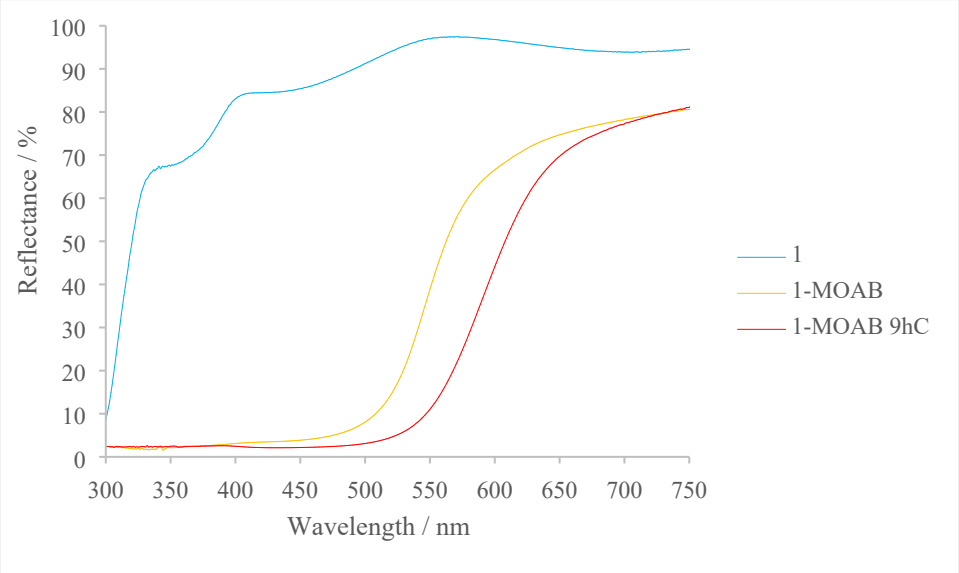

Figure S21. Solid-state UV-Vis diffuse reflectance spectra of **1**, **1**⊃MOAB and irradiated **1**⊃MOAB.

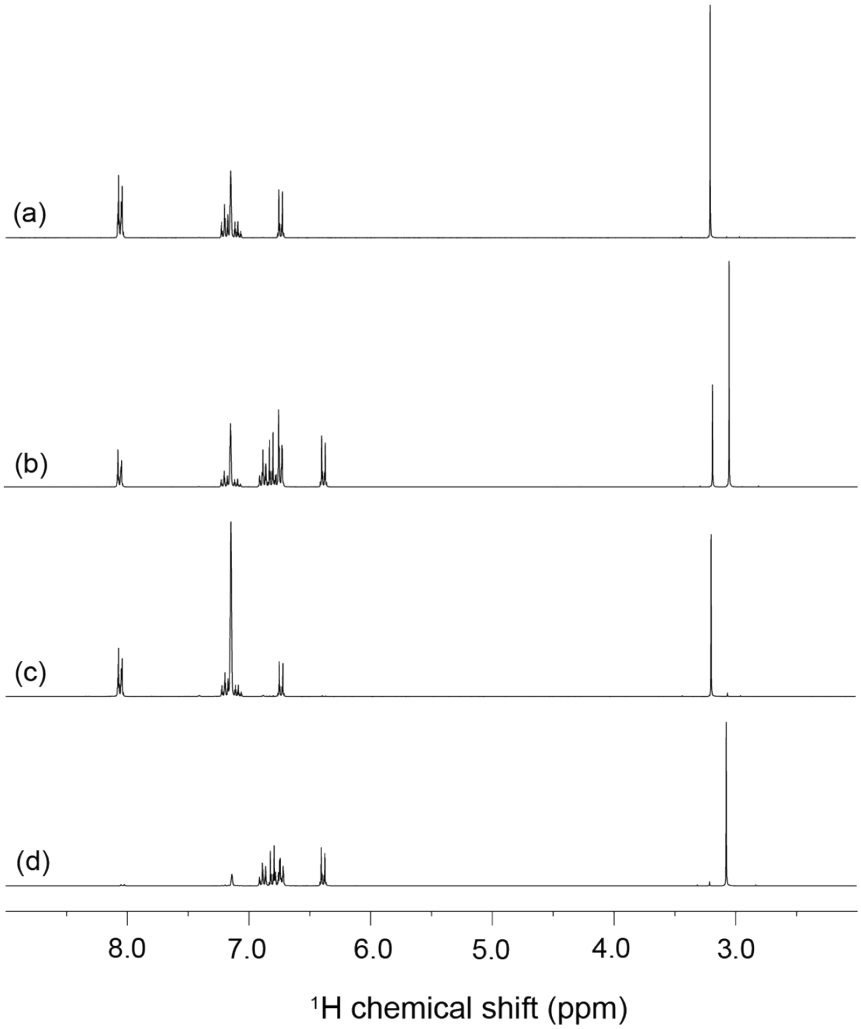

Figure S22. ^{1}H NMR spectra of a) E-MOAB, b) irradiated MOAB (2h), c) MOAB redissolved from **1**⊃MOAB c) before and d) after 540 minutes of irradiation, in benzene-d_6.

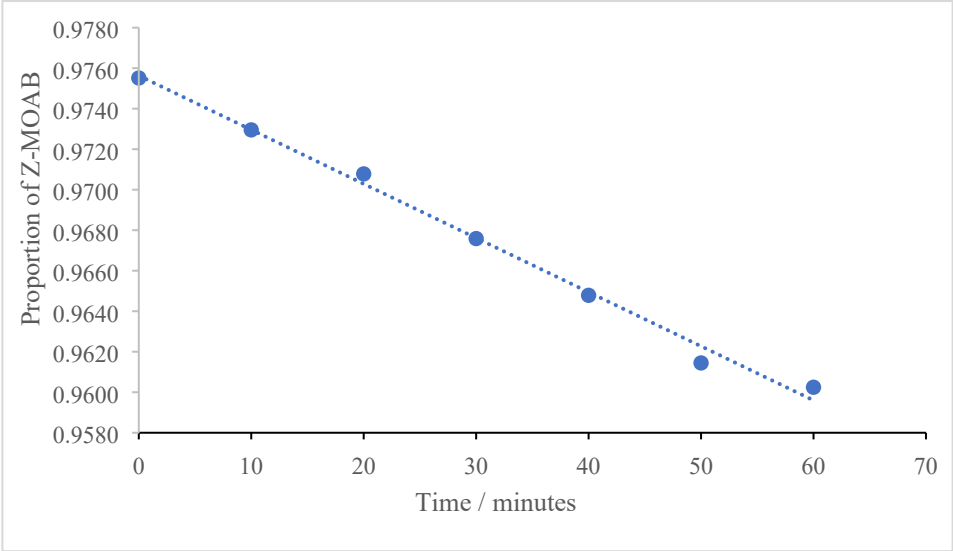

Figure S23. Plot of *Z*-MOAB population in benzene-d_6 as a function of time following irradiation at 365 nm.

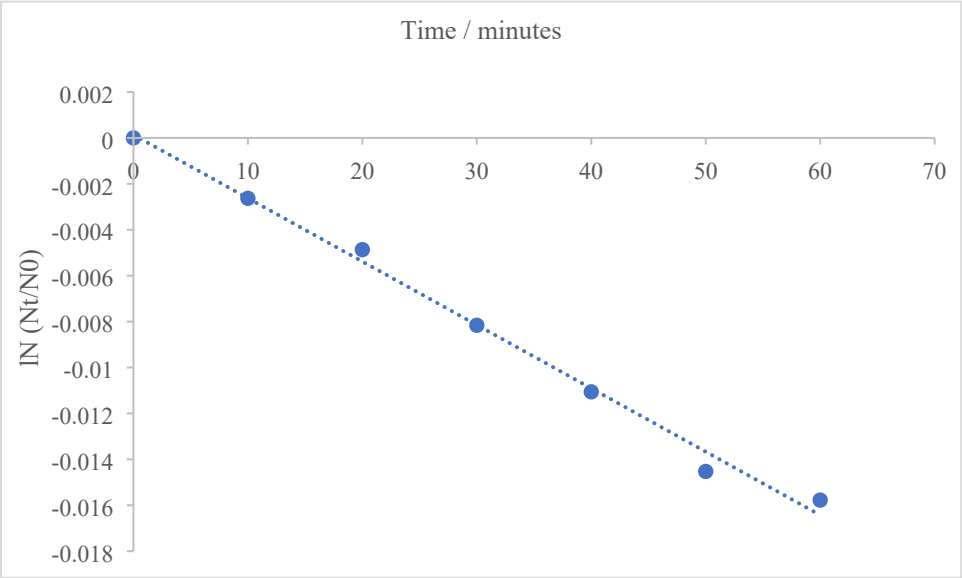

Figure S24. Plot showing $\ln(N_t/N_0)$ as a function of time, where N_0 is the population of *Z*-MOAB immediately after irradiation and N_t is the population of *Z*-MOAB at time *t*. Measurements were carried out in benzene-d_6 solution. The half-life of *Z*-MOAB in benzene solution was determined to be 38.5 hours.

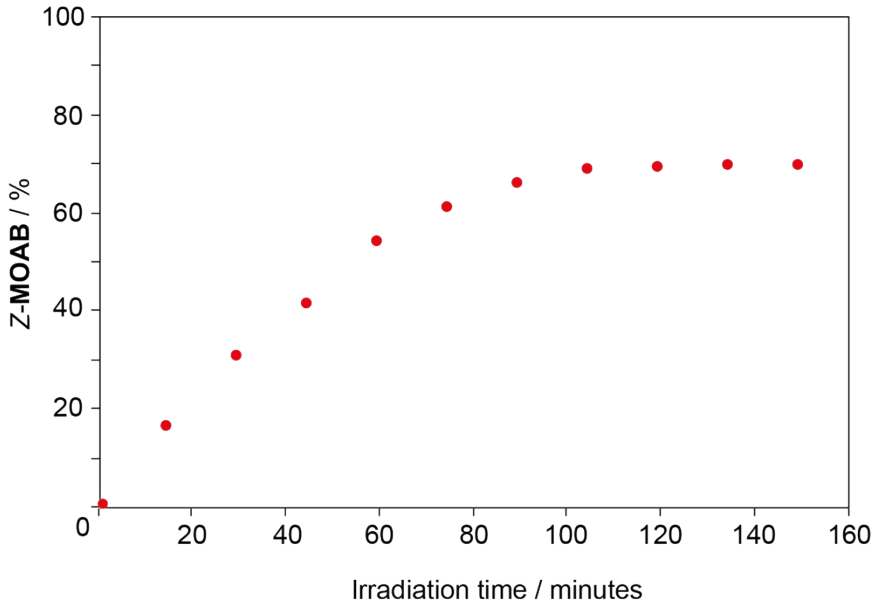

Figure S25. The increase in Z-MOAB proportion when MOAB irradiated in the crystalline state. A plateau is reached at 70% *Z*-MOAB.

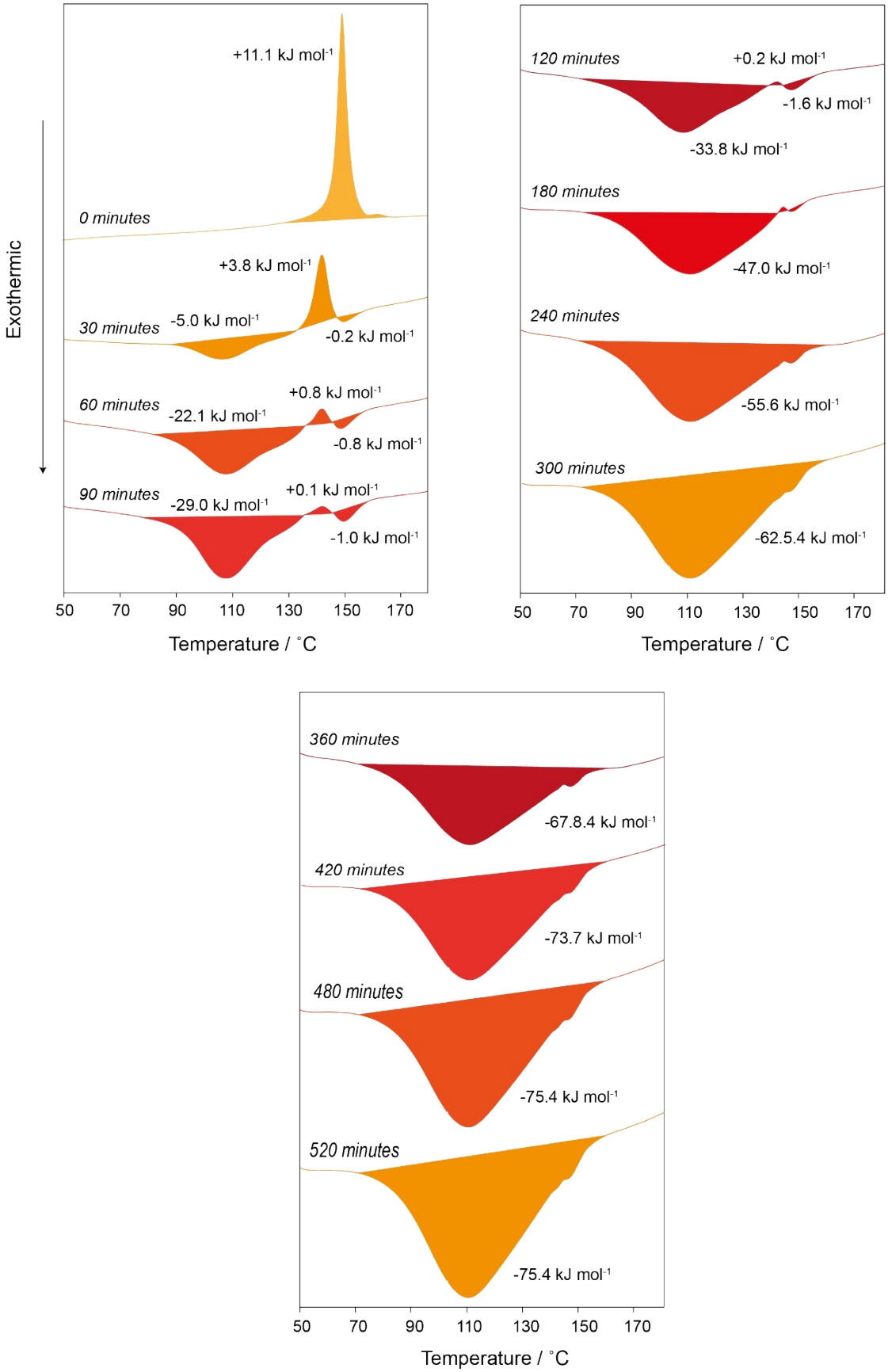

Figure S26. DSC thermograms of the first heating branch of **1**⊃MOAB with increasing irradiation time with a scan rate of 20 °C min^{-1}.

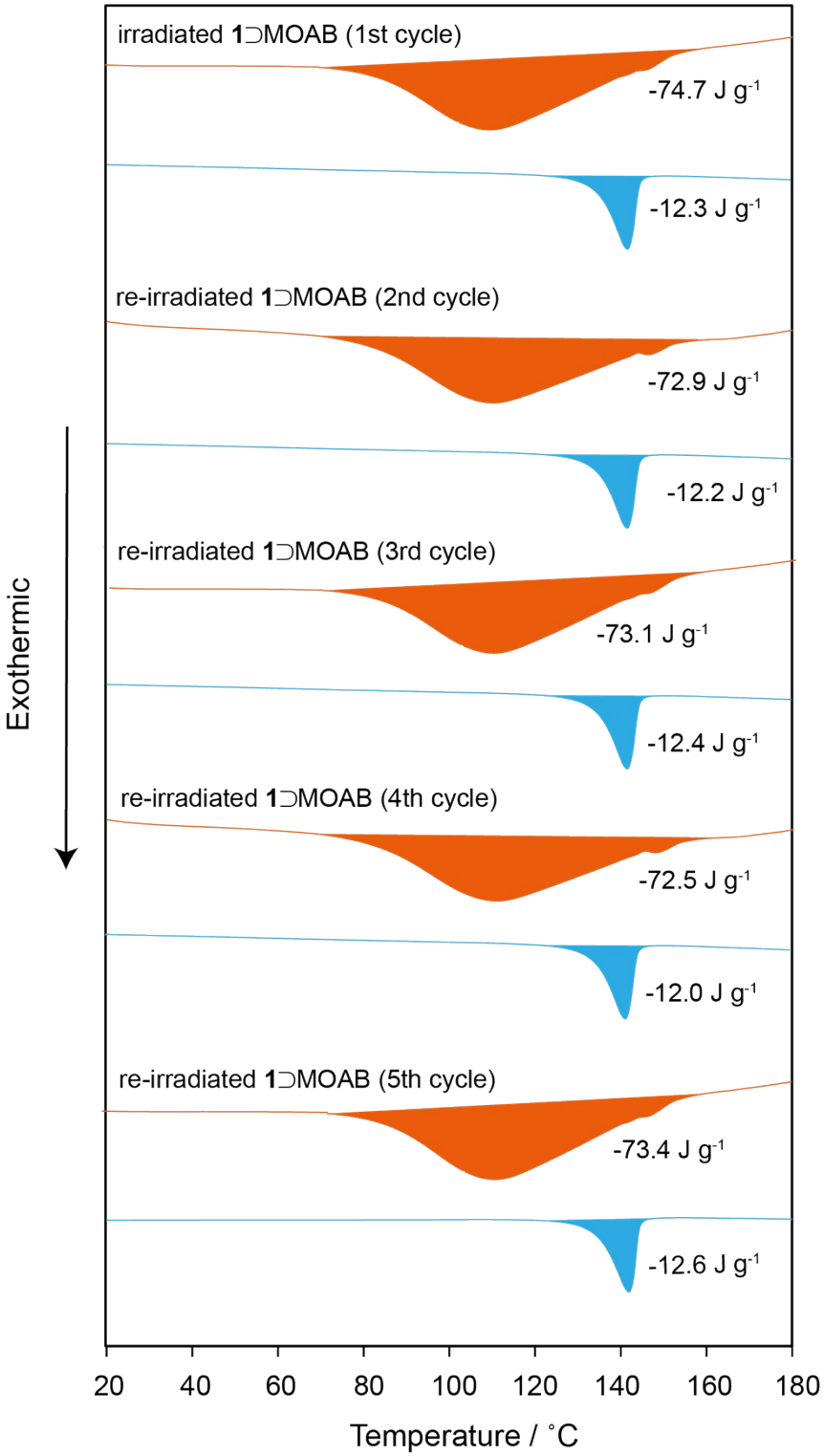

Figure S27. DSC cycling (irradiation/heat discharge) thermograms for **1**⊃MOAB. The material can be cycled up to five times without a loss in energy density.

Table S10. DFT calculated energy difference between *E*-MOAB and *Z*-MOAB were calculated using the CASTEP code where a single-molecule was confined in a 12 Å x 12 Å x 12 Å cell with fixed unit cell dimensions.

	Energy / eV molecule^{-1}	Energy / eV mol^{-1}	Energy / J mol^{-1}	Energy Density / J g^{-1}
E-MOAB	-3233.600200	-1.9473x10^{27}	-311995649.90	-1469944.17
Z-MOAB	-3232.887900	-1.9469 x10^{27}	-311926923.25	-1469620.37
Energy Difference	-0.712300	-4.2896 x10^{23}	-68726.65	-323.80

Table S11. Fractional Mass of MOAB in **1**⊃MOAB.

Sample	RMM	Fractional mass of MOAB
1	579.3	
1⊃MOAB	844.6	0.31

Table S12. Thermal data for the first heating branch **1**⊃MOAB with varying lengths of irradiation.

Time /	Exothermic (1)	Endothermic peak (1)/ J g^{-1}	Exothermic peak (2)/ J g-^{1}	Exothermic peak	Energy difference on heating

min	/ J g^{-1}			(3)/ J g-^{1}	branch / J g^{-1}
0	0.0	13.2	0	-12.7	0.5
30	-5.9	4.5	0	-12.6	-14.1
60	-26.2	0.9	-1.01	-12.5	-38.8
120	-40.0	0.2	-1.88	-12.5	-54.2
180	-55.6	0.0	-2.62	-12.6	-70.8
240	-65.9	0.0	0	-12.7	-78.6
300	-74.0	0.0	0	-12.3	-86.3
360	-80.2	0.0	0	-12.8	-93.0
420	-87.2	0.0	0	-12.2	-99.4
480	-89.2	0.0	0	-12.3	-101.5
540	-89.3	0.0	0	-12.5	-101.8

Table S13. Comparison for the experimental energy difference on the first heating branch and the calculated energy difference from *Z* to *E*-MOAB.

Time / min	*Z* / %	Correction for PSS / J g^{-1}	Calculated energy difference / J g^{-1}	Difference between calculated and experimental / J g^{-1}
0	0	0.00	0.00	0.50

30	0.13	-42.30	-13.29	-0.76
60	0.38	-123.64	-38.84	0.02
120	0.53	-172.45	-54.17	-0.06
180	0.69	-224.50	-70.53	-0.30
240	0.77	-250.53	-78.70	0.14
300	0.85	-276.56	-86.88	0.56
360	0.91	-296.09	-93.01	-0.02
420	0.95	-309.10	-97.10	-2.33
480	0.99	-322.12	-101.19	-0.34
540	0.99	-322.12	-101.19	-0.64

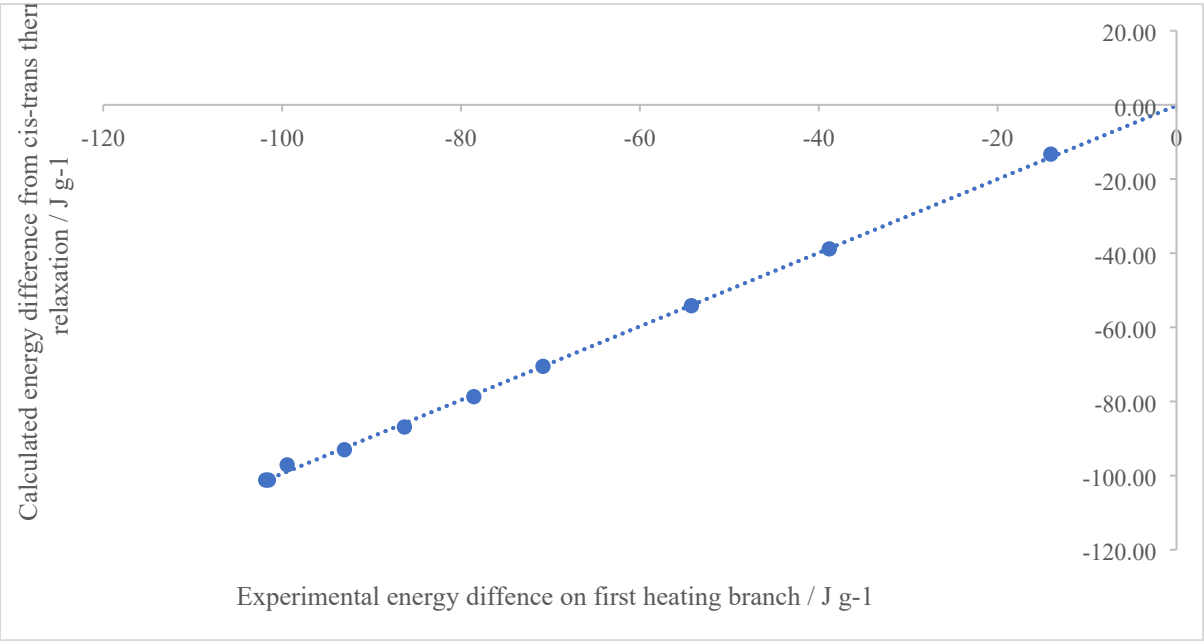

Figure S28. Relationship between the experimental energy difference on the first heating branch and the calculated energy difference due to *Z*-*E* thermal relaxation in **1**⊃MOAB.

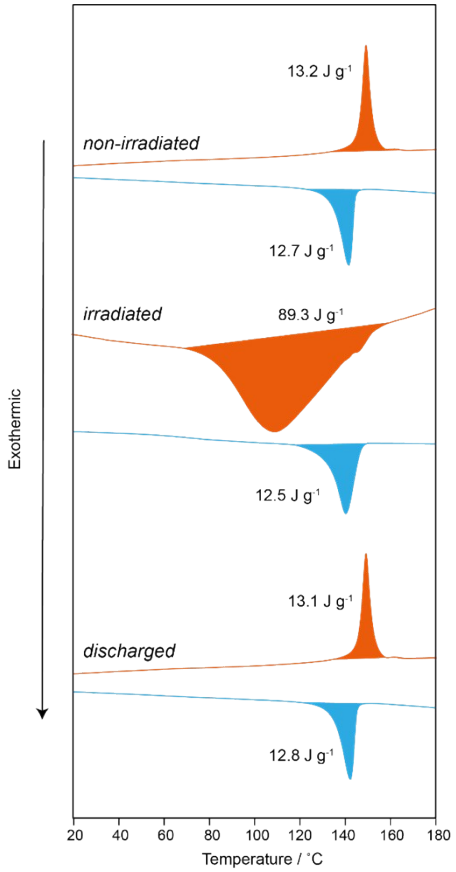

Figure S29. Successive DSC thermograms for (top) pristine **1**⊃MOAB (middle) irradiated **1**⊃MOAB and (bottom) thermally reconverted **1**⊃MOAB.

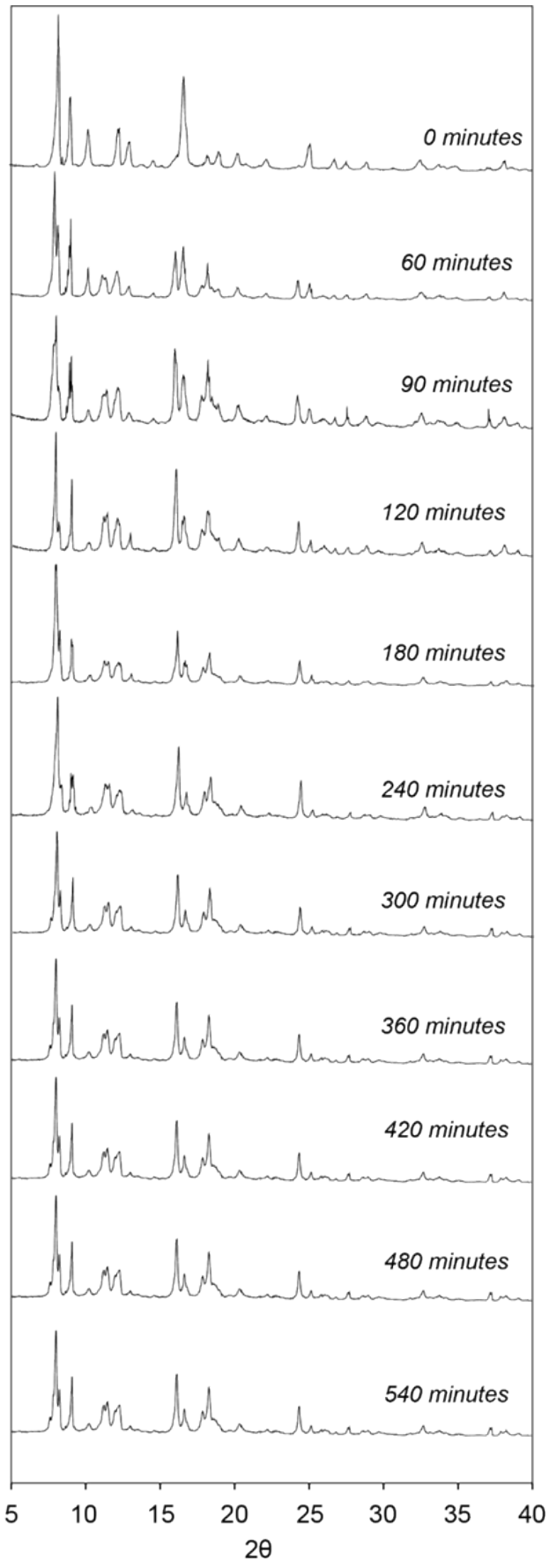

Figure S30. XRPD patterns of irradiated **1**⊃MOAB with specific times under 365 nm light.

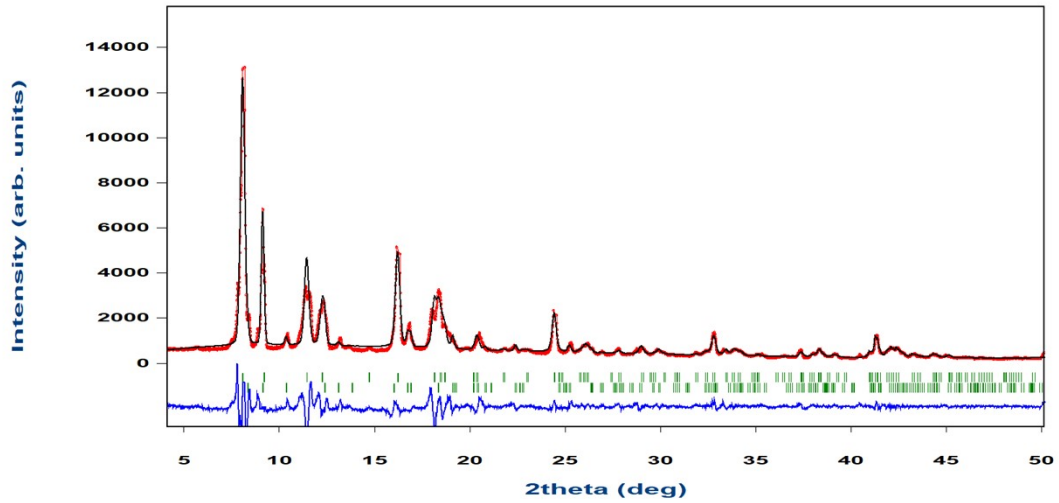

Figure S31. Le Bail fit of irradiated **1**⊃MOAB. Two phases were identified and the dominant phase's crystal system was found to be tetragonal. The lattice parameters were refined to be $a = b = 10.982(7)$ Å, $c = 9.619(3)$ Å, $\alpha = \beta = \gamma = 90°$, V = 1169.1(2) Å^3. The space group was found to be *P4/mmm*. The second crystal system was found to be orthorhombic. The lattice parameters were refined to be a =13.492(2) Å, $b = 17.129(4)$, $c = 9.679(8)$ Å, $\alpha = \beta = \gamma = 90°$, V = 2236.7(3) Å^3. The space group was found to be *Cmmm.* Which is consistent with the pre-irradiated phase. General formula $Zn_8C_{128}H_{120}N_{16}O_{32}$. The reliability (R) factor based on the powder profile *Rp* was 11.19 %.

Table S14. DFT calculated energy differences between *E* and *Z* isomers of ortho fluorinated azobenzenes (AB-F_x) which were reported to be occluded in MOFs.

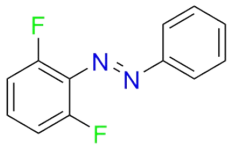

AB-F_2

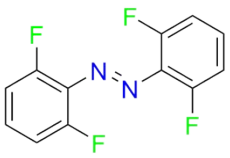

AB-F_4

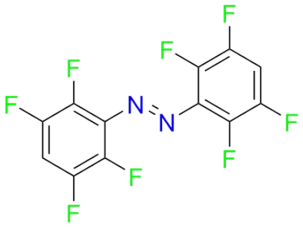

AB-F_8

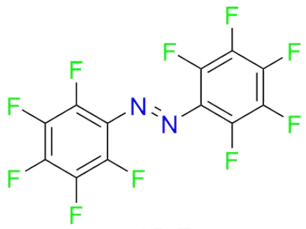

AB-F_{10}

AB-F_2	(energy/molecule) / (eV/molecule)	(energy/mole) / (eV/mol)	(energy/mol) / (J/mol)	kJ / mol
E isomer	-3894.29	-2.35E+27	-375743017.66	
Z-isomer	-3893.92	-2.34E+27	-375707122.46	
ED	-0.37	-2.24E+23	-35895.20	-35.90

AB-F_4	(energy/molecule) / (eV/molecule)	(energy/mole) / (eV/mol)	(energy/mol) / (J/mol)	kJ / mol
E isomer	-5184.86	-3.12E+27	-500264405.56	
Z-isomer	-5184.63	-3.12E+27	-500242155.10	
ED	-0.23	-1.39E+23	-22250.46	-22.25

AB-F_8	(energy/molecule) / (eV/molecule)	(energy/mole) / (eV/mol)	(energy/mol) / (J/mol)	kJ / mol
E isomer	-7765.80	-4.68E+27	-749287567.35	
Z-isomer	-7765.48	-4.68E+27	-749256674.16	
ED	-0.32	-1.93E+23	-30893.19	-30.89

AB-F_{10}	(energy/molecule) / (eV/molecule)	(energy/mole) / (eV/mol)	(energy/mol) / (J/mol)	kJ / mol
E isomer	-9055.96	-5.45E+27	-873769602.97	
Z-isomer	-9055.59	-5.45E+27	-873733471.02	
ED	-0.37	-2.26E+23	-36131.96	-36.13

Table S15. Calculated chemical shifts for a static molecule of *Z*-MOAB. The CASTEP code was used to geometry-optimise a single molecule within a unit cell with fixed dimensions of 12 x 12 x 12 Å before NMR parameters were calculated.

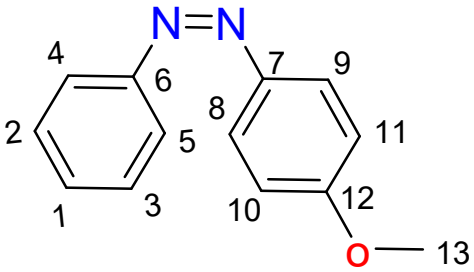

C site	σ_{iso}	Chemical shift / ppm
C1	44.6931	123.7669
C2	42.7124	125.7476
C3	40.1623	128.2977
C4	57.6192	110.8408
C5	44.2558	124.2042
C6	11.1773	157.2827
C7	21.865	146.595
C8	36.3859	132.0741
C9	53.4647	114.9953
C10	62.2751	106.1849
C11	55.6696	112.7904
C12	7.8567	160.6033
C13	117.8611	50.5989

Table S16. CASTEP-calculated chemical shifts for a dynamic molecule of *Z*-MOAB.

C site	σ_{iso}	Chemical shift / ppm
C1	44.6931	123.7669
C2/C3	41.43735	127.02265
C4/C5	50.9375	117.5225
C6	11.1773	157.2827
C7	21.865	146.595
C8/C9	44.9253	123.5347
C10/C11	58.97235	109.48765
C12	7.8567	160.6033
C13	117.8611	50.5989

Fast rotational averaging was accounted for by averaging chemical shifts for carbons on opposite sides of the six-membered rings. This simulates the effect of fast rotation of the six-membered rings around the C-N bond. In terms of the predicted chemical shifts, this averaging is also equivalent to fast pedal motion dynamics of the central N=N linkage – indeed rotation of the rings and pedal motion of the N=N linkage cannot be distinguished by this method.

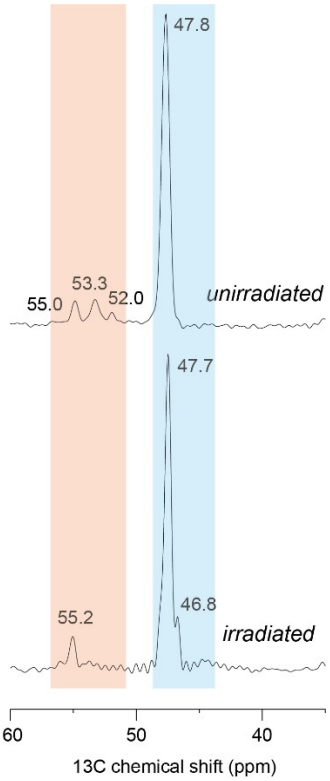

Figure S32. Comparison of the DABCO and methoxy regions of ^{13}C CPMAS NMR spectra of **1**⊃MOAB and irradiated **1**⊃MOAB.

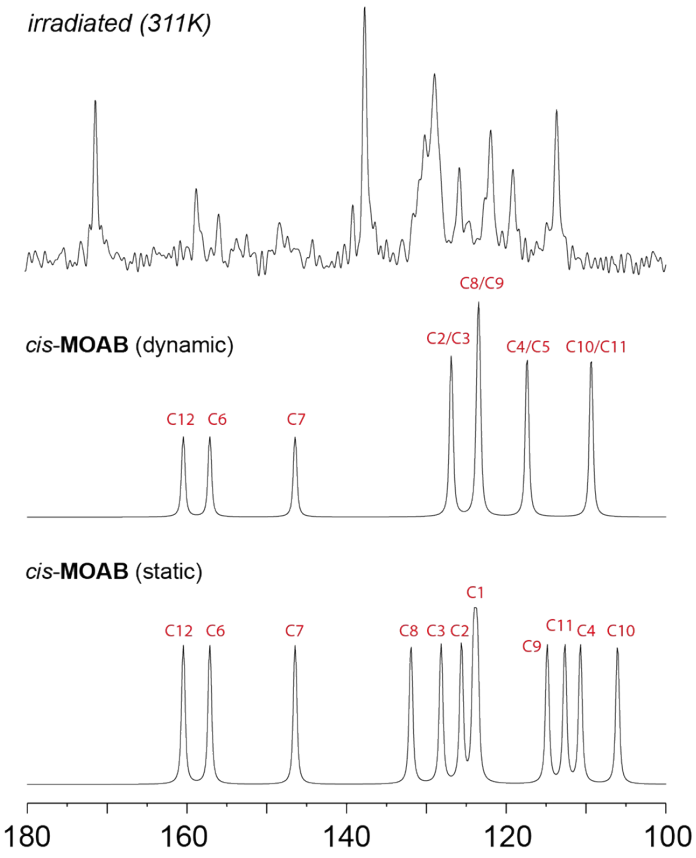

Figure S33. Comparison of the aromatic regions of ^{13}C CPMAS NMR spectra of irradiated **1**⊃MOAB to calculated chemical shifts for *Z*-MOAB.

Table S17. Population of *Z*-MOAB in **1**⊃MOAB measured at different time intervals over a period of one month.

hour	day	Fraction of Z-MOAB	Nt/N0	Ln(Nt/N0)	1/(Nt/N0)	1/(Nt/N0)1.5	1/(Nt/N0)2
0.00	0.00	0.98	1.00	0.00	1.00	1.00	1.00
1.00	0.04	0.97	0.99	-0.01	1.01	1.02	1.02
2.00	0.08	0.97	0.99	-0.01	1.01	1.02	1.02
3.00	0.13	0.96	0.98	-0.02	1.02	1.03	1.04
4.00	0.17	0.96	0.98	-0.02	1.02	1.03	1.04
5.00	0.21	0.95	0.97	-0.03	1.03	1.05	1.06
6.00	0.25	0.94	0.96	-0.04	1.04	1.06	1.09
7.00	0.29	0.94	0.96	-0.04	1.04	1.06	1.09
8.00	0.33	0.93	0.95	-0.05	1.05	1.08	1.11
24.00	1.00	0.85	0.87	-0.14	1.15	1.23	1.32
26.00	1.08	0.84	0.86	-0.15	1.16	1.25	1.35
28.00	1.17	0.83	0.85	-0.16	1.18	1.28	1.38
30.00	1.25	0.82	0.84	-0.17	1.19	1.30	1.42
46.00	1.92	0.75	0.77	-0.26	1.30	1.48	1.69
48.00	2.00	0.75	0.76	-0.27	1.32	1.51	1.73
50.00	2.08	0.74	0.75	-0.29	1.33	1.54	1.78
68.00	2.83	0.68	0.69	-0.37	1.45	1.74	2.10
69.00	2.88	0.67	0.69	-0.37	1.45	1.74	2.10
70.00	2.92	0.67	0.68	-0.39	1.47	1.78	2.16
71.00	2.96	0.67	0.68	-0.39	1.47	1.78	2.16
144.00	6.00	0.50	0.51	-0.67	1.96	2.75	3.84
216.00	9.00	0.41	0.42	-0.87	2.38	3.67	5.67
288.00	12.00	0.36	0.37	-0.99	2.70	4.44	7.30
360.00	15.00	0.32	0.33	-1.11	3.03	5.28	9.18
432.00	18.00	0.29	0.30	-1.20	3.33	6.09	11.11
504.00	21.00	0.27	0.28	-1.27	3.57	6.75	12.76
576.00	24.00	0.26	0.26	-1.35	3.85	7.54	14.79
648.00	27.00	0.24	0.25	-1.39	4.00	8.00	16.00

Figure S34. Decay plots for the *Z*-MOAB isomer with respect to order of decay.